

SCIENTIFIC REPORTS



OPEN

Improving superconductivity in BaFe₂As₂-based crystals by cobalt clustering and electronic uniformity

Received: 16 December 2016

Accepted: 17 March 2017

Published online: 19 April 2017

L. Li¹, Q. Zheng¹, Q. Zou², S. Rajput^{1,2}, A. O. Ijaduola³, Z. Wu^{2,4}, X. P. Wang⁵, H. B. Cao⁶, S. Somnath⁶, S. Jesse^{2,7}, M. Chi⁶, Z. Gai⁶, D. Parker¹ & A. S. Sefat¹

Quantum materials such as antiferromagnets or superconductors are complex in that chemical, electronic, and spin phenomena at atomic scales can manifest in their collective properties. Although there are some clues for designing such materials, they remain mainly unpredictable. In this work, we find that enhancement of transition temperatures in BaFe₂As₂-based crystals are caused by removing local-lattice strain and electronic-structure disorder by thermal annealing. While annealing improves Néel-ordering temperature in BaFe₂As₂ crystal ($T_N = 132$ K to 136 K) by improving in-plane electronic defects and reducing overall a -lattice parameter, it increases superconducting-ordering temperature in optimally cobalt-doped BaFe₂As₂ crystal ($T_c = 23$ to 25 K) by precipitating-out the cobalt dopants and giving larger overall a -lattice parameter. While annealing improves local chemical and electronic uniformity resulting in higher T_N in the parent, it promotes nanoscale phase separation in the superconductor resulting in lower disparity and strong superconducting band gaps in the dominant crystal regions, which lead to both higher overall T_c and critical-current-density, J_c .

After much research on cuprates and iron-based superconductors, the causes of unconventional superconductivity, and at a particular T_c , remain elusive. Iron-based superconductors can be created by chemical substitutions and charge doping of antiferromagnetic ‘parent’ materials that alter the nuclear and electronic structures, Fermi surfaces, carrier concentrations, and strength of spin fluctuations^{1–8}. As is well-known, AFe₂As₂ (A = Ca, Sr, Ba) parents (known as ‘122s’) have coupled antiferromagnetic striped order (Fe spins parallel along b -, antiparallel along a - and c -axes) and orthorhombic transitions below $T_N = T_s$ ⁹. However, there are variations of T_N in the literature within each family. For example, a BaFe₂As₂ crystal is reported to have $T_N = 134$ K^{10,11} that rises to $T_N = 140$ K after thermal annealing (at 700 °C)^{12,13}, while polycrystalline samples have $T_N = 140$ K¹⁴. Similarly, T_N values in SrFe₂As₂ can vary by 6 to 8 K^{13–15}. Moreover, CaFe₂As₂ crystals can be produced to have different T_N and even a non-magnetic ground state^{13,16}. We found that the thermal-annealing temperature matters and it can lead to homogenous crystalline lattices giving the highest coupled $T_N = T_s$ ¹³. As there are several parents and superconducting doping types, the cause of superconductivity for a particular dopant and at a particular superconducting temperature is unpredictable¹. Even looking within the family of BaFe₂As₂-based crystals and a particular doping level (x), T_c variations can be observed. For example, the specific heat results on Ba(Fe_{1-x}Co_x)₂As₂ with x = 0.045, 0.08, and 0.105 have shown that annealing (800 °C, 2 weeks) increases T_c between 2 to 5 K, decreases the residual linear term in specific heat (γ_0) in the superconducting state by as much as half while suppressing the Schottky-like contribution below 1 K^{17,18}. Moreover, the magnetic susceptibility of Ba(Fe_{1-x}Co_x)₂As₂ crystals with $0.04 \leq x \leq 0.14$ showed an increase of T_c values by ~1 to 3 K, with no significant change in superconducting Meissner or shielding fractions¹⁹. In addition, annealing (800 °C, 1 week) of Ba_{0.5}Sr_{0.5}(Fe_{1-x}Co_x)₂As₂ with x = 0.14 showed a T_c increase of 5 K in bulk properties, and a decrease in heat capacity γ_0 of more than half²⁰. In all of these

¹Materials Science and Technology Division, Oak Ridge National Laboratory, Oak Ridge, TN 37831, USA. ²Center for Nanophase Materials Sciences, Oak Ridge National Laboratory, Oak Ridge, TN 37831, USA. ³Department of Physics, University of North Georgia, Dahlonega, GA 30597, USA. ⁴Fujian Provincial Key Laboratory of Semiconductors and Applications, Collaborative Innovation Center for Optoelectronic Semiconductors and Efficient Devices, Department of Physics, Xiamen University, Xiamen, 361005, P.R. China. ⁵Chemical and Engineering Materials Division, Oak Ridge National Laboratory, Oak Ridge, TN 37831, USA. ⁶Quantum Condensed Matter Division, Oak Ridge National Laboratory, Oak Ridge, TN 37831, USA. ⁷Institute for Functional Imaging of Materials, Oak Ridge National Laboratory, Oak Ridge, TN, 37831, USA. L. Li, Q. Zheng and Q. Zou contributed equally to this work. Correspondence and requests for materials should be addressed to A.S.S. (email: sefata@ornl.gov)

examples, it is assumed that annealed crystals have improved crystallinity due to the release of residual strain, hence improve T_N or T_c . This paper offers an insight of complexity of $\text{Ba}(\text{Fe}_{1-x}\text{Co}_x)_2\text{As}_2$ quantum materials, which have intermingled effects of disorder, charge doping, electronic and crystal structure effects demonstrated by comparing results across multi-length scales using bulk techniques (diffraction, transport, magnetization), local probes (spectroscopy, microscopy) and theoretical input. Our results suggest that annealing improves electronic uniformity and T_N in the parent, while it promotes clustering of cobalt dopants at nanoscales to form more pinning sites and improved J_c in the superconductor with more uniform and stronger regions of superconducting gaps that give higher overall T_c . The latter result is most interesting, specifically in relation to some of the literature work on nanoscale chemical, electronic, and spin separation in superconductors. In fact, the overall strength of antiferromagnetism or superconductivity below a particular transition temperature in a crystal is produced by a complex combination of many details such as chemical, lattice, and spin structures, and defects that affect electronic states. For example, superconductivity in iron-arsenides can be tied to the c -lattice parameter changes with chemical substitution⁸, and also on chemical disorder and clustering^{21, 22}, non-hydrostatic pressure²³, and strain effects²⁴. Regarding local-scale measurements on high-temperature superconductors, X-ray absorption fine structure (EXAFS) technique has found that nanoscale lattice fluctuations play a crucial role in causing T_c ²⁵. Moreover, scanning tunneling microscopy (STM) finds evidence of changing Fermi surfaces that are correlated with strong local-doping variations²⁶, and anisotropic scattering by impurity states at atomic-scale electronic structures²⁷. Using micro X-ray diffraction imaging, non-uniformity of short-range charge-density-wave and quenched disorder are found to arise from dopants and strain²⁸. In iron-selenide superconductors, techniques such as angle-resolved photoemission spectroscopy (ARPES), transmission electron microscopy (TEM) and edge structure analyses, STM, and X-ray nanofocus diffraction have shown mesoscale phase separations²⁹, iron vacancies^{30, 31}, magnetic domains magnetism^{32, 33}, can diminish superconductivity.

In this manuscript, we report on two sets of crystals, each set with same average composition of x with either antiferromagnetic order or superconductivity. Within each set, each crystal has slightly different T_N or T_c value achieved by thermal annealing. Here we explore each pair of “as-grown” versus “annealed” antiferromagnetic BaFe_2As_2 or superconducting optimally cobalt-doped BaFe_2As_2 , in order to understand reasons for their improved transition temperatures with annealing. We analyze the bulk properties in crystals, and also their nanoscale variations in the atomic-resolved and real-space lattice and electronic structures that get averaged by them. We report that higher transition temperatures in annealed crystals are due to the higher overall electronic and chemical uniformity, as expected. However, surprisingly, cobalt dopants can get precipitated out of the main crystalline matrix that yields larger electronically connecting regions with stronger superconductivity and better pinning for annealed crystal.

Results and Discussions

Although there is no distinct change in the average compositions of each as-grown versus annealed $\text{Ba}(\text{Fe}_{1-x}\text{Co}_x)_2\text{As}_2$ crystal, the average structures change only in-plane, as will be shown below in a -lattice parameter variations, and local smearing effects along the ac plane. Figure 1a (top) shows typical size and quality of $\text{Ba}(\text{Fe}_{1-x}\text{Co}_x)_2\text{As}_2$ crystals that were used for our annealing studies, and the room-temperature tetragonal crystal structure that is made of covalently-bonded layers of (Fe/Co)As in the ab -plane separated by Ba ions along the c -axis. Figure 1a (bottom) shows the variation in cobalt composition across a crystal with an average composition of 2.4% cobalt; this wavelength dispersive X-ray spectroscopy results shows that cobalt amount is non-uniform on the micrometer scale changing by $\sim 0.1\%$. For all the crystals studied here, the x chemical composition is reported after averaging the results of energy dispersive X-ray spectroscopy (EDS) on 3 random spots ($\sim 90\text{ }\mu\text{m}$ diameter each). Figure 1b shows the refined lattice parameters versus x , from X-ray diffraction of powdered crystals. As expected for as-grown $\text{Ba}(\text{Fe}_{1-x}\text{Co}_x)_2\text{As}_2$ crystals^{10, 34}, a -lattice constant remains mainly invariant while c -axis shrinks with increasing x due to smaller Co ions substituting for Fe. However, upon annealing, the c -lattice parameter does not change while the a -lattice parameter changes slightly, decreasing for the parent while increasing for optimally-doped $x=0.063$ crystal. This negligible c -parameter change of less than 0.01 \AA was reported for $x=0$ annealed crystals¹³. Figure 2a shows evidence of peak broadening and lattice distortions for two sets of annealed crystals from axial photographs of single-crystal X-ray diffraction. We show the simulation for an overlay of a section of [101] layer to produce this smearing effects of lattice due to these results: for $x=0.063$, a small misalignment along [010] of ~ 1.0 degrees can give the evident peak broadening; for $x=0.146$ a twin law rotation along [010] by 2.4 degrees can produce peak splits. This result is also reflected in atom displacement along the crystallographic c direction, demonstrated in Fig. 2b, found by refining the full dataset for $x=0.063$. The amplitude of this distortion causes the increase of arsenic height by $\sim 0.0026\text{ \AA}$ for annealed $x=0.063$, although the averaged c -lattice parameter stays the same. The strain effect along the ac plane may be due to clustering of cobalt atoms in small local regions as is evident from local microscopy results (explain below).

For the annealed BaFe_2As_2 crystal and as evident below, the coupled antiferromagnetic and structural transition temperatures improve while the crystal becomes more homogeneous. Figure 3a represents temperature-dependent results of magnetic susceptibility (χ), heat capacity (C), and Hall coefficient (R_H). In the bulk properties, the shift of anomalies due to antiferromagnetic transition from $T_N=132\text{ K}$ to 136 K is similar to those reported¹³. There is no change in the heat capacity Sommerfeld coefficient ($\gamma_0 \approx 6\text{ mJ/K}^2\text{mol}$) upon anneal. The R_H results of as-grown crystal is similar to those reported^{35, 36}, although the magnitude of the R_H increases for annealed crystal probably due to higher electron mobility. In Fig. 3b, the neutron diffraction results for the changes in nuclear and magnetic structures are shown. Comparing the tetragonal, T , (220)_T Bragg peak for BaFe_2As_2 at 4 K and 200 K, there was not sufficient resolution to observe the peak splitting similar to others reported^{37, 38}. However, the intensity change with temperature due to peak broadening or extinction effect indicates the tetragonal-orthorhombic structural transition (T_s), as seen by the temperature dependence of peak intensity. The stronger intensity change in annealed crystal indicates the larger tetragonal-orthorhombic lattice

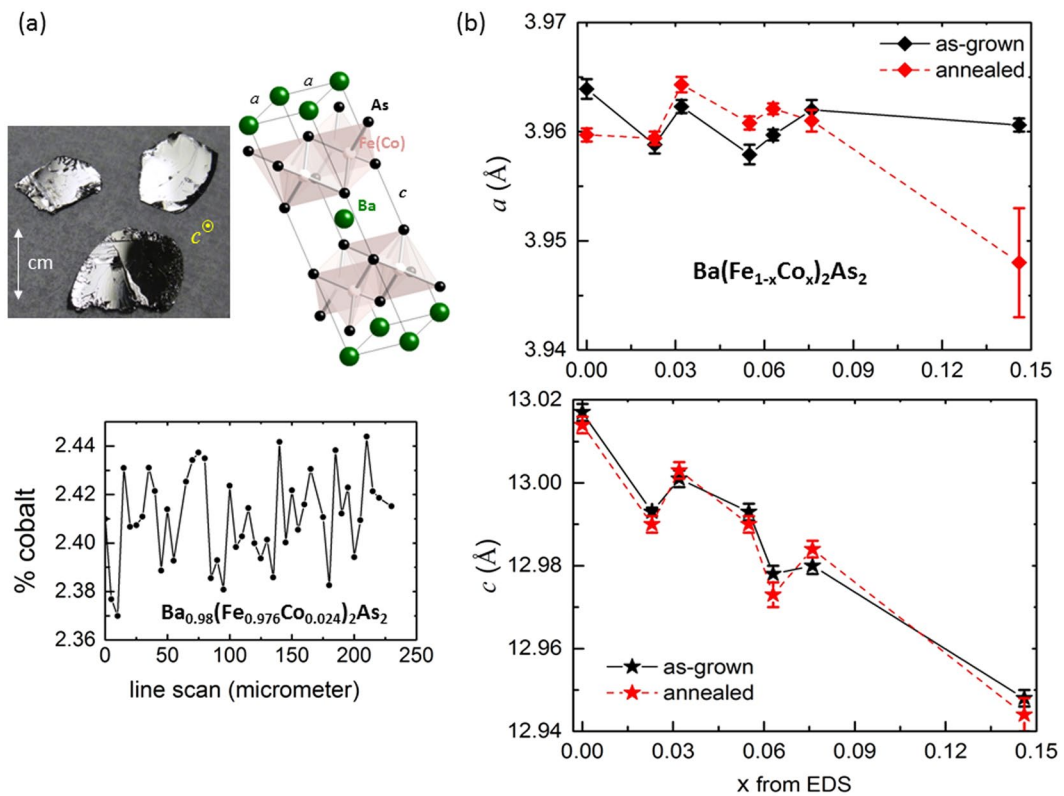


Figure 1. Small variations of cobalt concentrations within a crystal, and changes in a -lattice parameters with annealing of $\text{Ba}(\text{Fe}_{1-x}\text{Co}_x)_2\text{As}_2$ crystals. (a) (Top) Typical size and quality of as-grown $\text{Ba}(\text{Fe}_{1-x}\text{Co}_x)_2\text{As}_2$ crystals, and room-temperature tetragonal crystal structure of $\text{Ba}(\text{Fe}_{1-x}\text{Co}_x)_2\text{As}$, with unit cell shown in solid black line; (Bottom) A line scan across a crystal with average composition of $\text{Ba}_{0.98}(\text{Fe}_{0.976}\text{Co}_{0.024})_2\text{As}_2$, assuming full occupancy of layers. (b) The refined a - and c -lattice parameters at room temperature, from powdered crystals with doping levels (x). The level of x does not change upon annealing, within error.

distortion compared to as-grown. The peak intensities of the magnetic Bragg reflection $(\frac{1}{2}\frac{1}{2}\frac{5}{2})_T$ versus temperature are also plotted here. We confirm that structural and magnetic transitions start at 132 K while for annealed crystal they occur at \sim 136 K, similar to transitions inferred from bulk properties. Our neutron diffraction results are also consistent with the combined result of magnetic susceptibility and X-ray diffraction measurements that showed that increase in structural and magnetic phase transitions are coincident to less than 0.1 K³⁹. Figure 4a gives the STM results of a large-scale image of as-grown parent crystal surface; atomically-resolved images have already been reported⁴⁰. We see hundred nanometers wide flat terraces on both cleaved as-grown and annealed BaFe_2As_2 crystalline surfaces; the most common step terrace height is 0.75 nm, which is about half of a unit cell in c -axis. Zooming on the flat terrace reveals spatial bright and dark nanoscale regions shown in Fig. 4b; line profile across the surface indicates a height variation of less than 1 Å (inset). These height variations are too small to be caused by missing atoms in the top layer, and hence most likely related to electronic inhomogeneity due to the fact that STM image is a convolution of spatial variation in the topographic height and the local density of states. The insets of Fig. 4c show the local electronic property comparison of the as-grown vs annealed crystals measured in a region with step edges at 90 K. The averaged dI/dV spectra over the whole area for both as-grown and annealed crystals exhibit V-shape (black and purple curves), which is consistent with earlier reported tunneling spectroscopy measurements on the parent compound⁴¹. However, a detailed analysis reveals different dI/dV spectra in different areas on the surface. The local dI/dV curves as well as the cluster image in Fig. 4c show large varieties for the as-grown sample but are quite similar in the annealed sample, although the STM morphologies of the two samples are almost the same. The areas with same color in the cluster image represent the same electronic behavior. The closer the color, the similar the property. To calculate the cluster image, firstly, we filtered the measured I-V data via SVD filtering followed by a Gaussian filter. Next, we smoothed each I-V data via a median filter of size 3, and numerically computed the dI/dV . Next, we performed a moving window average of 3×3 pixel areas to reduce the noise in the dI/dV data. Finally, we performed K-means clustering to find the spatial distribution of the principal responses in the data. For the as-grown crystal (Fig. 4c, top), in some areas, the dI/dV spectra (dark blue curve) exhibits a peak near the Fermi level at 25 mV surrounded by two dips at -125 mV and 85 mV, in contrast to having a single minimum at 65 mV in the adjacent area. In another area (green curve), peak at 25 mV is suppressed and result in a more U-shaped dI/dV spectra. The origin of the peak near the Fermi level is unknown at present, and has been also observed in gold-doped BaFe_2As_2 ⁴². Nevertheless, these results indicate that as-grown BaFe_2As_2 crystal is electronically inhomogeneous at local scales, and the averaging of differential conductance spectra over a large area hides information. A similar analysis done with the dI/dV map taken on

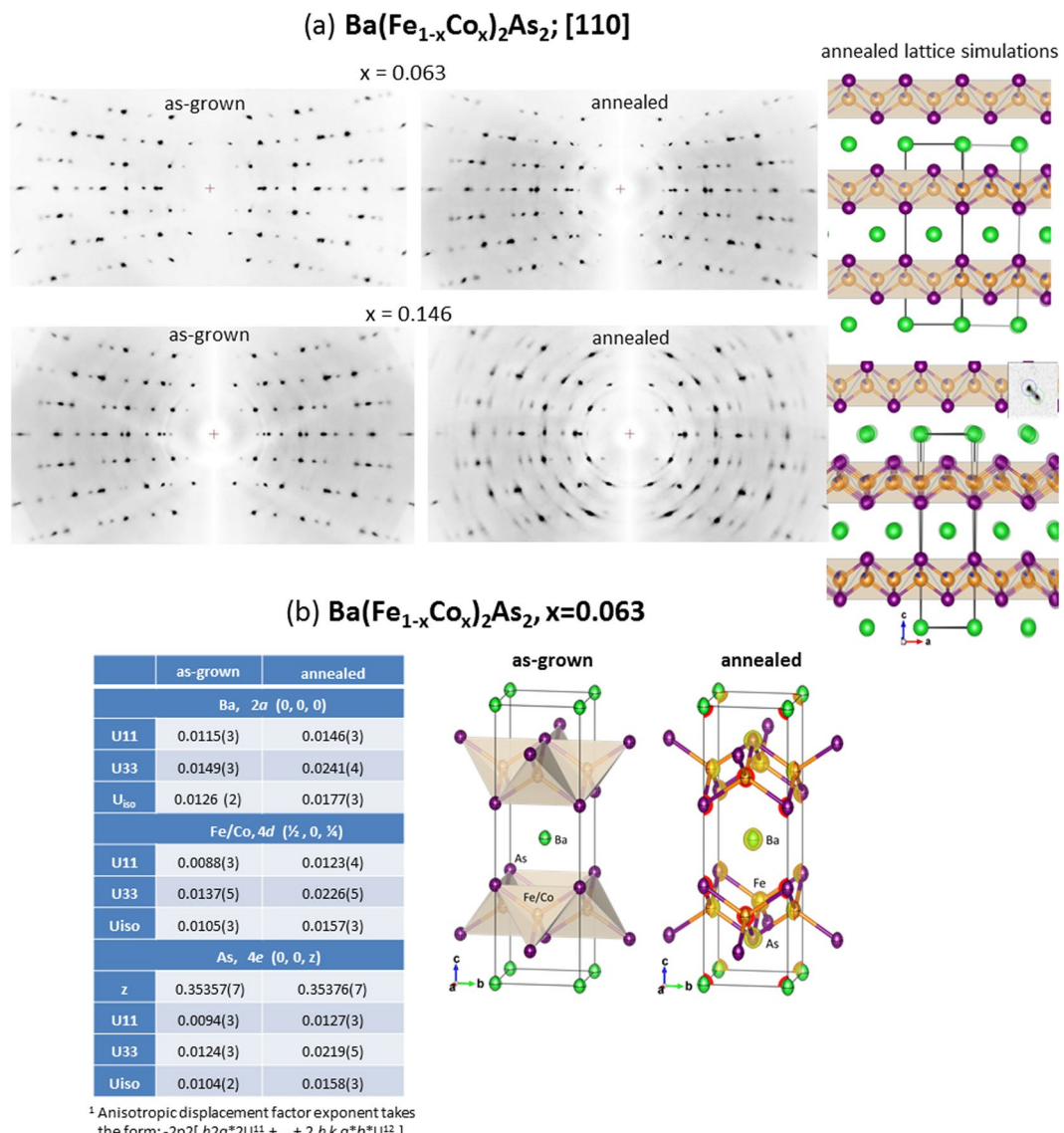


Figure 2. Smearing effects in annealed crystals demonstrated by single crystal X-ray diffraction on $\text{Ba}(\text{Fe}_{1-x}\text{Co}_x)_2\text{As}_2$ crystals. (a) (Left) [110] axial photographs computed from omega-scan images on as-grown compared to annealed crystals, for $x = 0.063$ and 0.146 . (Right) Overlay a section of [101] layers to simulate the effects of lattice misalignment for the annealed crystals: Top is demonstrating misalignment along [010] by ~ 1.0 degrees for $x = 0.063$; bottom is showing twin law rotation along [010] by ± 2.4 degrees, with upper-right giving the peak split, which may result for $x = 0.146$. (b) Table shows the refined atomic displacement parameters¹ (\AA^2) for as-grown and annealed crystals of $\text{Ba}(\text{Fe}_{1-x}\text{Co}_x)_2\text{As}_2$ with $x = 0.063$. A site occupation ratio of 0.937:0.063 obtained from elemental analysis for Fe/Co atoms at $4d$ site was used in structural refinement. Polyhedral drawing of the crystal structure of these crystals at the 90% ellipsoid level, is shown on the right. For annealed crystal, there is an overlay of electron density (e \AA^{-3}) with iso-surface level shown at 5% of the maximum.

the annealed crystal (in Fig. 4c) shows that annealed sample is comparatively electronically homogeneous as the dI/dV spectra taken at various locations on the surface are qualitatively similar to the one averaged over the whole area (black curve). All the curves show a V-shape with local minimum at 45 mV. However, occasionally a peak type feature appeared near the Fermi level similar to red curve on annealed BaFe_2As_2 sample with variation in the peak position from -15 mV to 35 mV. The atomic resolution aberration-corrected scanning transmission electron microscopy (STEM) imaging has been reported on various members of iron-based superconductors along different crystallographic projections⁴³ with high angle annular dark-field detector (HAADF) mode, in which the image's intensity is proportional to $Z^{1.6-2}$. Figure 4d shows a typical plane-view of STEM-HAADF image of BaFe_2As_2 . The beam parallel to [001] projection resolves the Ba + As, and Fe columns appearing in bright and medium light, respectively. Although no analyzes of such images were performed along many microns, we suspect that there is some local strain relief for annealed crystalline lattice. For example, our previous study on CaFe_2As_2 parent annealed (350°C) crystal with $T_N = 168(1)$ K showed a strain relief through local 0.2 \AA atomic displacements found in-plane HAADF images⁴⁴. We can conclude that annealing of BaFe_2As_2 results in a more

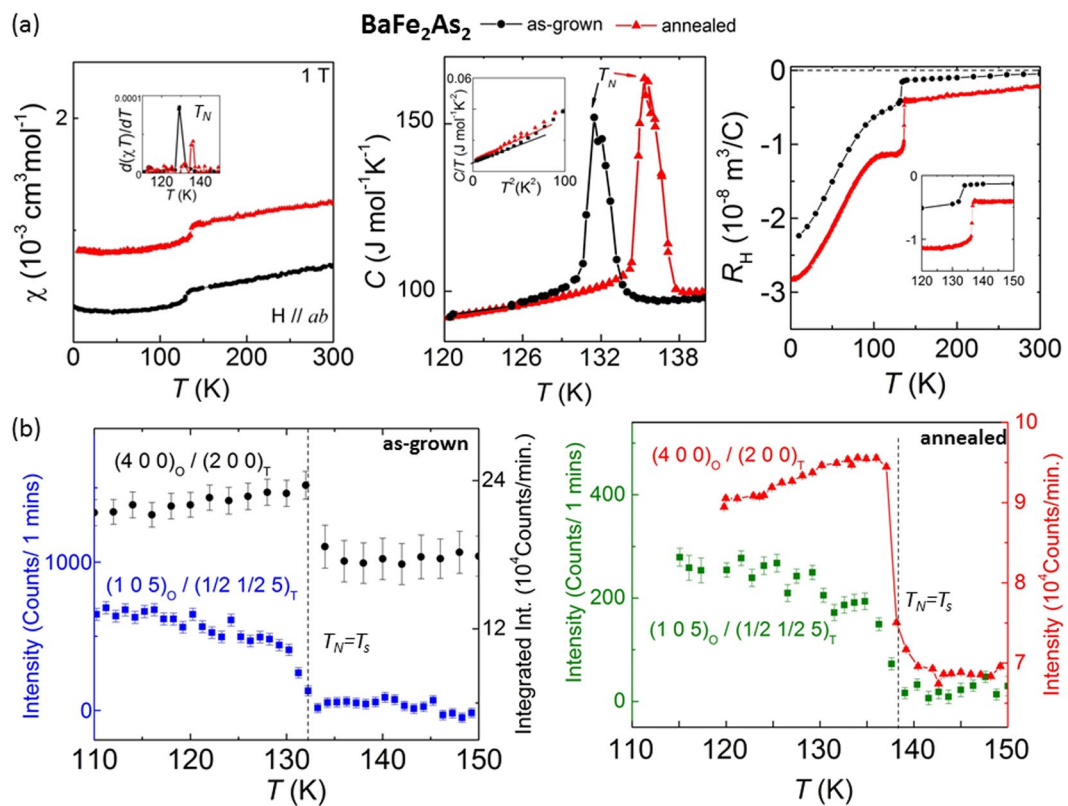


Figure 3. The increase in the coupled antiferromagnetic (T_N) and structural (T_s) temperatures upon annealing BaFe_2As_2 crystal. For BaFe_2As_2 crystals of as-grown (in black) and annealed (in red), temperature dependence of anomalies in (a) magnetic susceptibility (χ), heat capacity (C) and Hall coefficient (R_H), and (b) structural and magnetic Bragg neutron reflections. In (b), temperature-dependence of the peak intensity change of the tetragonal ($\frac{1}{2}\frac{1}{2}\frac{5}{2}$)_T magnetic reflection and (200)_T structural peaks are shown.

electronically homogeneous crystal, which is most probably due to lattice strain relief, confirmed here from STS statistical analyses here on local areas.

In order to gain insight on T_N changes for BaFe_2As_2 , our first principles calculations here indicate a strong sensitivity of magnetism to structure, consistent with the previously shown strong magnetoelastic coupling⁴⁵. As in this previous work, we have computed the magnetic ordering energy, defined as the difference in energy ΔE between the ground-state ‘stripe’ structure and the ‘checkerboard’ structure of the parent compound and several structural modifications, as presented in Table 1. Within a mean-field approximation, this energy difference is proportional to the T_N . We note that while the structural modifications described here might be envisioned as application of pressure, one may view them as arising from changes in average lattice parameters caused by synthesis condition or thermal annealing. Indeed, in Fig. 1b we see an approximate 0.1% decrease in planar lattice parameter (within the tetragonal phase) from annealing. Consistent with this experimental fact, we find that the application of uniform compressive pressure (“hydrostatic”), or along the c -axis (“ c -axis uniaxial”) substantially decreases the ordering energy, and hence the Néel temperature in these calculations. For in-plane changes, however, the situation is more complex, and indeed we find that the application of 1% compression along the ferromagnetic Fe-Fe alignment direction (“FM uniaxial”), combined with a 1% tensile stress along the antiferromagnetic Fe-Fe direction, in fact *increases* the ordering energy by 9.2%. Such an increase is roughly consistent with the observed 3% increase in T_N we observe from the annealing, particularly when one considers that the observed decrease in planar lattice parameters would generally be expected to increase the exchange interaction. The suggestion of these results is that slight structural changes can be responsible for the observed T_N change.

For superconducting $\text{Ba}(\text{Fe}_{1-x}\text{Co}_x)_2\text{As}_2$ crystals annealing produces sharper and higher T_c values, while for optimally-doped crystal critical current density (J_c) also increases. In the annealed crystal, there is probably nano-scale phase separation of cobalt-depleted and cobalt-rich regions within the same crystal, diminishing the overall distribution of chemical and electronic disorder, leading to the formation of more uniform electronic regions of enhanced or no superconductivity, as is demonstrated below. Figure 5 shows temperature-dependent results of resistivity (ρ) and magnetic susceptibility (χ) for under-doped $x = 0.023$, optimally-doped $x = 0.063$, and over-doped $x = 0.146$ crystals. For $x = 0.023$ (Fig. 5a), annealing reduces the overall magnitude of ρ and χ , while shifting the T_N value from ~ 90 K to 93 K. For $x = 0.063$ (Fig. 5b), annealing shows both higher and sharper T_c and a lower normal-state resistivity, and although χ magnitude is increased slightly at lower temperatures and 1 Tesla, the Meissner fraction is slightly increased at 10 Oe with improvement of T_c . For $x = 0.146$ (Fig. 5c), annealing produces bulk superconductivity at higher temperature of ~ 12 K, even though the absolute values of ρ and χ

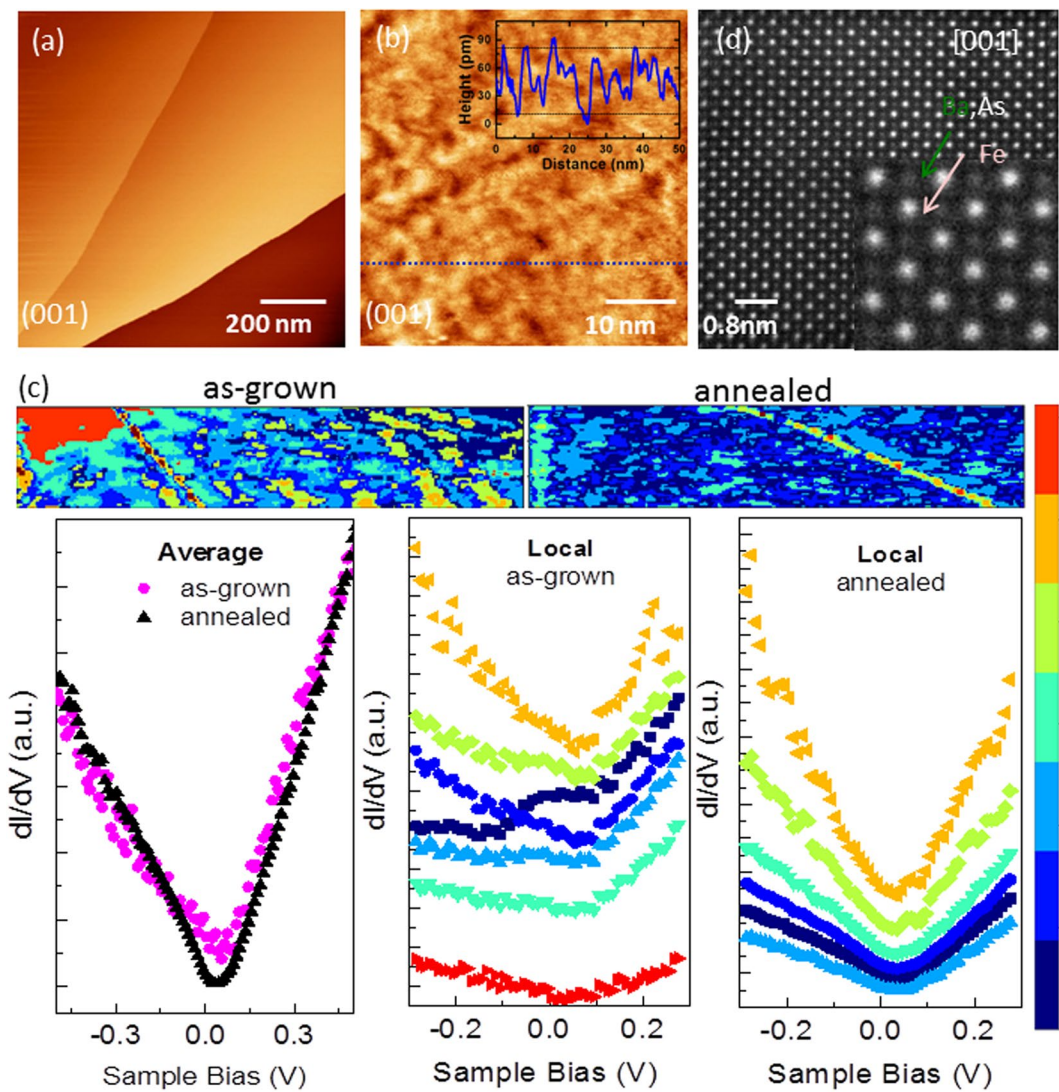


Figure 4. The improved electronic homogeneity in annealed BaFe_2As_2 crystals. For as-grown BaFe_2As_2 , in-plane topographic STM image of (a) cleaved surface showing large atomically flat terraces ($V_s = -0.5$ V, $I_t = 20$ pA), (b) a close-up of a flat terrace with tunneling conditions $V_s = -0.5$ V, $I_t = 20$ pA, and inset is a line profile taken along the dashed blue line. (c) For as-grown and annealed BaFe_2As_2 , cluster images constructed from I-V curves are shown in the top (1000×300 nm). The average dI/dV spectra for the whole areas as well as the local dI/dV spectra for different clusters for both samples are shown in the bottom. The cluster image and the spectra share the same color bars on the right side, the closer the color, the similar the spectra. (d) For BaFe_2As_2 , a typical STEM-HAADF image of BaFe_2As_2 along [001] orientation.

Scenario	Δa (%)	Δb (%)	Δc (%)	ΔE (meV/ Fe)	% change from baseline
baseline	—	—	—	49.41	—
hydrostatic	-1	-1	-1	42.14	-14.7
<i>c</i> -axis uniaxial	+1	+1	-2	42.29	-14.6
FM uniaxial	-1	+1	—	53.97	+9.2
AF uniaxial	+1	-1	—	44.78	-9.4

Table 1. Calculated ordering energies for several structural modifications of BaFe_2As_2 parent, as could be produced via hypothetical lattice-parameter changes.

increase. A broad superconducting transition temperature in magnetic susceptibility was observed frequently for overdoped crystals, ascribed to most inhomogeneous cobalt-doping composition¹⁹. For annealed crystal with

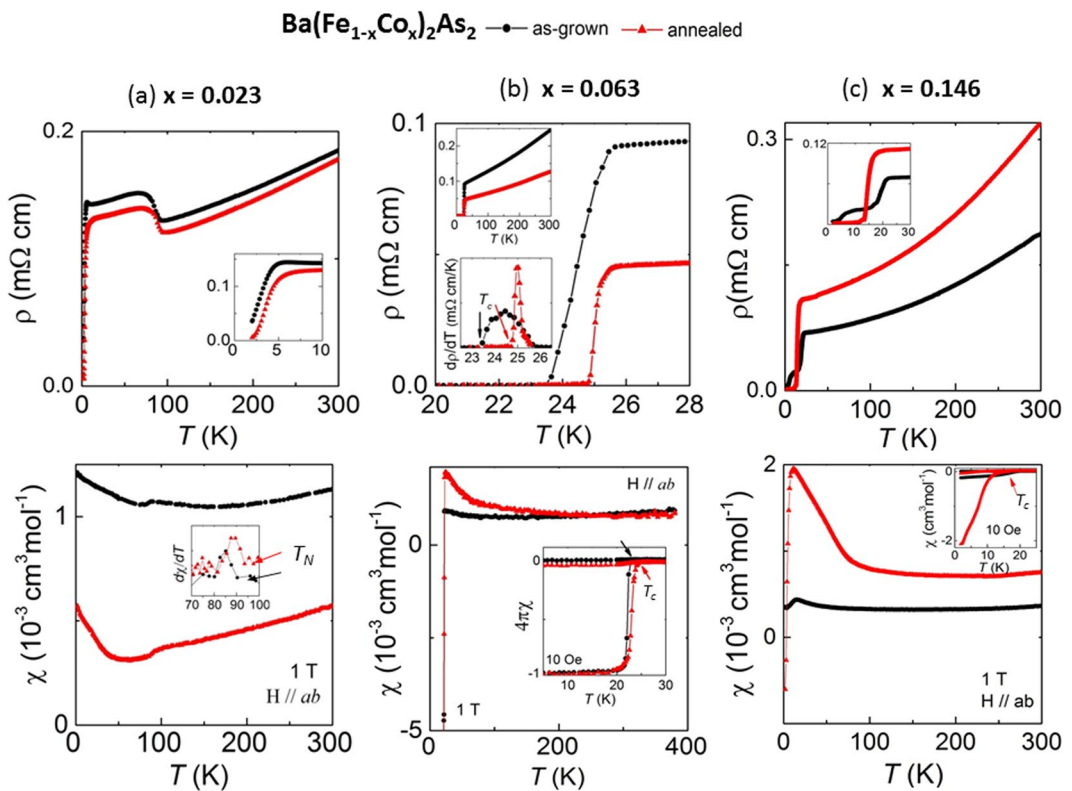


Figure 5. The improvement in superconducting critical temperature (T_c) signals upon annealing $\text{Ba}(\text{Fe}_{1-x}\text{Co}_x)_2\text{As}_2$ crystals. For $\text{Ba}(\text{Fe}_{1-x}\text{Co}_x)_2\text{As}_2$ crystals of as-grown (in black) and annealed (in red), temperature dependence of resistivity (ρ ; top row) and magnetic susceptibility (χ ; bottom row) for (a) $x = 0.023$, (b) $x = 0.063$, and (c) $x = 0.146$.

$x = 0.063$, the rise in T_c is confirmed with anomalies in heat capacity (not shown), although there is no change in the electronic contribution ($\gamma \approx 3 \text{ mJ/K}^2\text{mol}$). Figure 6a shows improved J_c values for annealed crystals. J_c values are calculated at two different temperatures below T_c , and as a function of applied field H . The ‘fishtail’ J_c peak effects have been observed and reported in similar crystals^{46–49}; J_c is fairly constant at very low fields (up to 0.07 T), then starts to drop off (from about 0.08 to 0.6 T), and can gradually increase and fall again. This feature may indicate the presence of nanoscale phase separation into regions of weaker superconductivity, perhaps caused by an inhomogeneous distribution of the cobalt⁵⁰. Also for both crystals, J_c does not fall off too rapidly with the application of magnetic field; this implies its weaker dependence on H . The J_c in the annealed crystal is more than four times larger than that measured in the as-grown crystal at very low fields, while it is about three times larger at intermediate and higher fields. The annealed sample has a self-field J_c of about 1 MA/cm² at 5 K, which compares favorably with those measured in Co-doped BaFe_2As_2 epitaxial films deposited on LSAT and MgO substrates at 1–4 MA/cm² at 4 K⁵¹. Other J_c values of 0.4 MA/cm² at 4.2 K⁴⁶ and 0.26 MA/cm² at 5 K⁴⁸ have also been reported. Further insight into the pinning strength can be achieved when the temperature dependence of J_c is analyzed, shown at an applied field $H = 0.2$ T (Fig. 6b). Superconductors with a weak pinning behavior such as ours usually exhibit an exponential decrease in J_c with temperature at low applied fields, owing to the low effectiveness of point-like defects against thermal activation of vortices⁵². Strong pinning mechanisms, such as correlated disorder pinning instead exhibit more smooth temperature dependence. The enhancement in J_c in the annealed sample is attributable to cobalt clustering seen as defects in the plane view (seen in microscopy images, below), giving rise to better pinning. Such chemical non-uniformity should effect local electronic structures. Although the surfaces of BaFe_2As_2 are known to reconstruct, the superconducting gaps from different surface reconstruction are expected to be almost identical since the superconductivity is a global property and ~ 3 nm coherence lengths are found for these materials^{53–55}. In fact, for $\text{Ba}_{0.5}\text{Sr}_{0.5}(\text{Fe}_{1-x}\text{Co}_x)_2\text{As}_2$ with $x = 0.073$ as-grown crystal ($T_c = 17$ K), scanning tunneling microscopy/spectroscopy (STM/S) results of at 4.3 K found inhomogeneous gap values from about 3 meV down to 0 meV²⁰. For $\text{Ba}(\text{Fe}_{1-x}\text{Co}_x)_2\text{As}_2$ crystals, Fig. 7 demonstrates STM/S results at 4.2 K and the smaller variability in superconducting gap maps for the annealed $x = 0.063$ crystal. After the cold cleavage (~ 100 K), the samples were immediately transferred into low-temperature STM. Figure 7a shows the topographic images acquired from the set of crystals. While the large-scale morphologies of the surfaces are essentially the same for the two, the detailed atomic-level structures may show some discrepancies from cleavages, consistent with the reported cleavage dependent controversies from the literature⁵³. To reveal the real space superconductor gap information from the crystals, the current-imaging-tunneling spectroscopy (CITS) were carried out; Fig. 7b gives the normalized dI/dV spectroscopy averaged over the whole areas of (a). By fitting the dI/dV spectroscopies using the standard functional form from Dynes *et al.*⁵⁶, the gap Δ maps can be deducted from the CITS images,

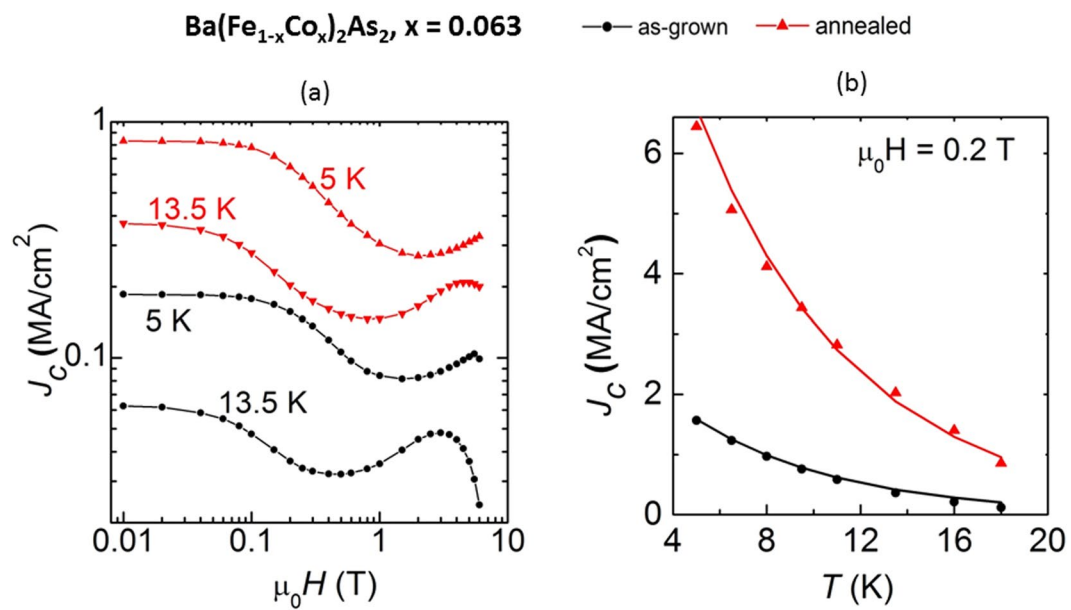


Figure 6. The increase in superconducting critical current density (J_c) for annealed optimally-doped $\text{Ba}(\text{Fe}_{1-x}\text{Co}_x)_2\text{As}_2$ crystal. For $x=0.063$ and as-grown (in black) and annealed (in red) crystals, (a) field dependence of critical current density (J_c) below T_c , and (b) temperature dependence of J_c at 0.2 Tesla.

as shown in Fig. 7c. In the map of the as-grown crystal, much more dispersed electronic regions with different gaps are seen, while in the map of the annealed crystal, there are larger areas of non-superconducting clusters and the green regions with gap ~ 5 meV is more prominent and are connected. The statistic histogram distributions of the superconducting gaps in Fig. 7d show that the peaks of the gap are located at 6.6 meV and 5.0 meV, respectively for as-grown versus annealed. The histograms are the statistic results from around 3100 dI/dV curves from each crystal, with full-width-at-half-maximum (FWHM) of 4.9 and 4.0. Skewness is smaller in the as-grown sample (0.45) comparing to the annealed sample (0.70), indicating a better symmetry of the probability distribution; the kurtosis of the two samples are 1.8 vs 2.1, describing a similar peak shape of the distributions, but the FWHM of the as-grown is broader than the annealed sample. The spike at lowest gap is shown in the statistic histogram distributions, but was not included in the quantitative measure for the FWHM, center, skewness and kurtosis. The main difference between the two gap distributions is a much higher probability at $\Delta=0$ for the annealed crystal, supporting the higher pinning sites suggested by higher J_c . The smaller FWHM for the annealed sample means narrower gap distribution, consistent with the sharper superconductivity transition, shown in bulk properties. The extracted corresponding gap-to- T_c ratios $R=2\Delta/k_b T_c$ from the peaks of the gaps are 6.7 and 4.6, respectively, using $T_c=23$ K and 25 K for the as-grown and annealed crystals. Although in the weak coupling s -wave BCS theory the R is a constant of 3.53, the d -wave symmetry of the order parameter in cuprate superconductors makes the ratio to a larger value of 4.28 and higher⁵⁷. Furthermore, recent studies found R of electron or hole doped BaFe_2As_2 can vary from 2.2 to 10.3^{32,54,58–61}. Figure 8 gives evidence of chemical clustering in annealed superconducting crystal. STEM results can give bulk chemical nature, as they are the average signal of many atomic unit cells along the beam direction. As shown in Fig. 8a, the low-magnification image along [001] that which STM/S were analyzed, show differences: uniform contrast in as-grown crystal indicates chemical homogeneity (top), however, the nano-clusters (dark regions) in size of around 10 nm or smaller in annealed crystal indicates chemical non-uniformity (bottom) that can be separated by more than 100 nm. Typical atomic resolution image on either crystal is shown in the inset of top image, and shows no visible defects. Electron energy loss (EEL) spectra and EELS spectroscopy mapping collected at thin areas are shown in Fig. 8b, indicating chemical inhomogeneity for annealed crystal and two types of nano-clusters: one type of nano-cluster regions shows weaker Ba signal (top spectra; collected on Titan at 300 kV), while the other one reveals stronger Ba signal (bottom spectra; collected on Nion 100 at 100 kV). The EELS mapping of the latter type was performed and is shown in Fig. 8c, demonstrating such chemical inhomogeneity. Since $\text{Co } L_{2,3}$ edge overlaps with Ba M -edge, the weaker or stronger Ba M -edge in the nano-clusters could be the result of less or more cobalt. In support of this and as evident in refinements of unit cells above, c -parameter should increase if there is less cobalt substituted in the 122 structure, i.e. it is possible that cobalt precipitates out by forming grain boundaries, leaving the main matrix of annealed crystal having less cobalt. Therefore, in the annealed crystal, there is evidence of cobalt clustering into cobalt rich and deleted regions giving sharper and slightly higher T_c . Such nano-size chemical phase separation of cobalt may be responsible for the higher J_c value.

With regards to the effects of annealing on the superconducting state, it is rather remarkable that annealing increases T_c while significantly decreasing the average superconducting gap size. Usually a smaller gap correlates with a decreased T_c , given that most theories predict a constant ratio of the gap to T_c , within a weak-coupling regime. One clue to the origin of this unusual behavior can be found in the averaged dI/dV curves (Fig. 7b). One

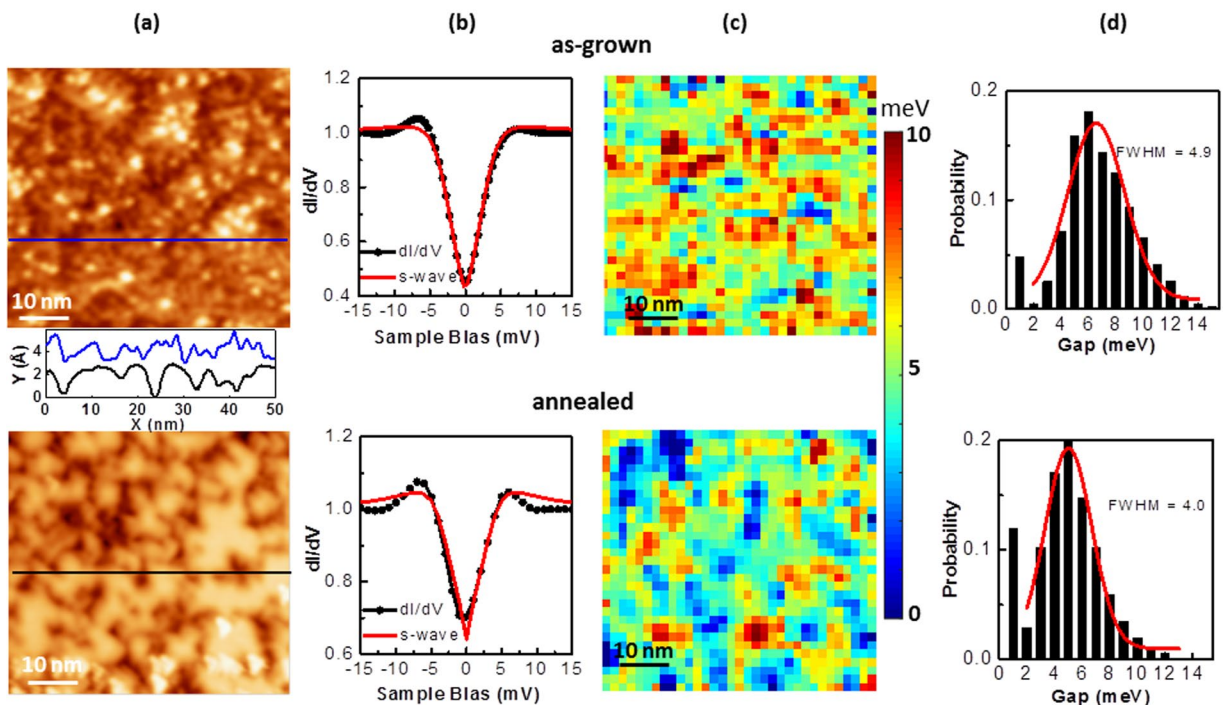
Ba(Fe_{1-x}Co_x)₂As₂, x = 0.063

Figure 7. Narrower superconducting gap distributions, and more uniform superconducting electronic clusters for annealed optimally-doped Ba(Fe_{1-x}Co_x)₂As₂ crystal. For crystal with x = 0.063, and as-grown (top row) and annealed (bottom row) crystals cleaved *in-situ* at 100 K: (a) topographic STM images with sample-bias voltage V_b = 20 mV and tunneling current I_t = 100 pA for as-grown crystal, and V_b = 25 mV and I_t = 100 pA for annealed crystal, and 50 nm × 50 nm areas. (b) normalized dI/dV spectroscopy averaged over the whole areas of (a) (1024 datasets), with s-wave fitting of the data in red. (c) Superconducting gap maps derived from dI/dV spectra from (a) with modulation V_{rms} = 0.5 mV at 973 Hz. (d) Histogram distributions of the gap Δ of (c) respective gap maps, with Gaussian fitting in red. Line profiles along the blue and black lines of (a) are shown in-between the two images. The two lines are offset for clarity.

notes that the coherence peaks located at approximately ± 5 mV are significantly sharper in the annealed sample, and reach greater heights and form better-connected percolating regions. In these samples, these features are ultimately controlled by two factors: the amount of quasiparticle scattering in the sample (discussed below), as well as by the distribution of gap values. A sample with a narrower distribution of gap values, as we observe in the annealed sample, will also tend to have higher and sharper coherence peaks when the resulting dI/dV curves are averaged over many locations. Quasiparticle scattering is typically modeled by the parameter Γ introduced by Dynes. In a pure s-wave sample, the scattering modeled by Γ does not typically affect T_c substantially, if the scattering originates in a non-magnetic manner (Anderson's theorem). However, for more complex pairing symmetries such as s_{+-} or d -wave, such scattering can greatly impact T_c , with the magnitude of the effect dependent both upon the specific pairing symmetry as well as the strength of the scattering. We therefore suggest, in addition to inducing a narrower distribution of gap values, that the annealing in some manner reduces the quasiparticle scattering, and thereby the pair-breaking effects of such scattering, thus raising T_c . Complicating such an interpretation, however, is the substantially larger fraction (12%) of small (< 1 meV) gap regions in the annealed state (Fig. 7d), relative to the 5% in the as-grown crystal. One would typically associate a smaller Γ with a more homogeneous chemical and electronic structure, yet this larger small-gap fraction argues in the opposite direction. It is possible, though clearly unproven here, that these small gap regions somehow play an important role in the global superconducting behavior, such as by donating charge to the system, despite apparently impeding superconductivity at the local level. In fact, the enhancement of superconductivity at the boundary between strongly underdoped and overdoped regions has been observed in the past. For example in the cuprates, a record T_c of 50 K was reported in bilayer of strongly overdoped non-superconducting La_{1+x}Sr_xCuO₄ (x = 0.45), and the top layer of underdoped insulating La₂CuO₄. The enhanced superconductivity was confined to a very thin (~ 2 unit cells) interfacial layer, and believed to be the transfer of charge from the overdoped to the underdoped layer across the interface, providing optimal doping without introducing chemical disorder. Similar to this case, cobalt clustering in the annealed crystal may create regions made up of cobalt-enriched and cobalt-depleted regions with reduced quenched disorder analogous to the case of under/overdoped La₂CuO₄ sublattices⁶².

This research has allowed us to gain understanding of how competing local and averaged chemical and electronic structures control antiferromagnetic ordering temperature or cause bulk zero resistance below a temperature in single crystals. In the present work, we have looked at a few crystal compositions within Ba(Fe_{1-x}Co_x)₂As₂

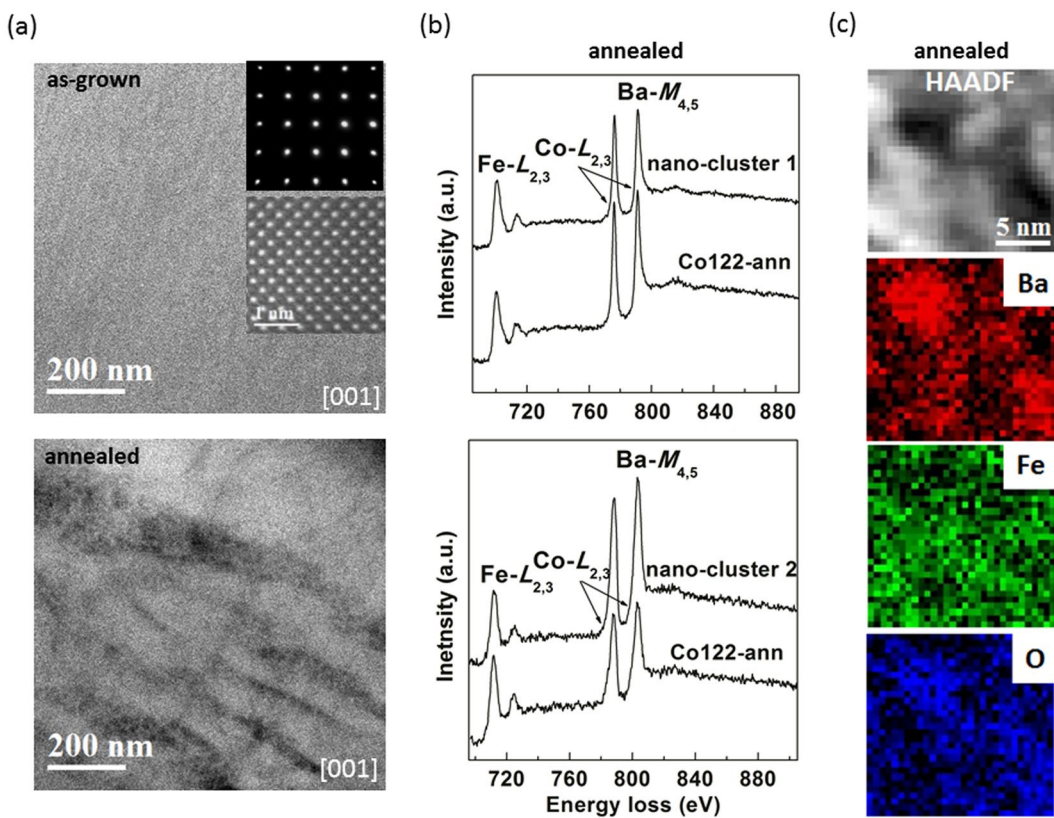


Figure 8. Evidence of chemical clustering in annealed optimally-doped $\text{Ba}(\text{Fe}_{1-x}\text{Co}_x)_2\text{As}_2$ crystal: (a) Typical STEM HAADF images along [001] showing chemical homogeneity for as-grown (top) versus nano-clusters in annealed (bottom) crystals, the insets are typical electron diffraction patterns and atomic resolution image. For annealed crystals, two different types of nano-clusters showing chemical inhomogeneity as revealed by (b) EEL spectra and (c) EELS mapping for one type of nano-clusters.

system, and refined the bulk compositions and structures using X-ray spectroscopy and diffraction techniques, and also used microscopy and spectroscopy experiments to investigate local chemical and electronic structure disorder within crystals. Higher T_N seems to be arising from more globally ordered lattice with shorter averaged a -lattice parameter and homogeneous electronic structure upon annealing, and higher T_c and J_c in optimally-doped crystal is correlated to less electronic structure variation, cobalt clustering giving larger average a -lattice parameter. Hence, annealing improves transition temperatures in $\text{Ba}(\text{Fe}_{1-x}\text{Co}_x)_2\text{As}_2$ crystals by removing the lattice strain and much of the electronic-structure disorder/disparity; this is simply summarized in Fig. 9.

Methods

Synthesis and preparation of crystals. Single crystals of $\text{Ba}(\text{Fe}_{1-x}\text{Co}_x)_2\text{As}_2$ were grown out of self-flux, and FeAs and CoAs binaries synthesized similar to our previous reports⁶³. Selected crystals, with no visible surface flux, were sealed under vacuum in silica tubes, and then heated in box furnaces. The crystals of $x=0$ were annealed at 700 °C for one month, and $x>0$ were annealed at 800 °C for two weeks. Although low-temperature magnetic susceptibility results (<30 K) showed identical effect on the enhancement of T_c for $x=0.07$ crystals annealed in various atmospheres of argon, air, or in vacuum¹⁹, we still opted for vacuum-annealing. For parent and optimally-doped crystals, the same ‘piece’ of each crystal was carefully shared and measured across all techniques. For example, resistivity of an annealed piece was measured prior to annealing, and small areas of each piece was analyzed via local techniques.

X-ray diffraction. Powder X-ray diffraction (XRD) data on numerous $\text{Ba}(\text{Fe}_{1-x}\text{Co}_x)_2\text{As}_2$ were collected on an X’Pert PRO MPD diffractometer ($\text{Cu } K_{\alpha 1}$ radiation, $\lambda=1.540598 \text{ \AA}$); the lattice parameters were refined by least-squares fitting within the program package WinCSD⁶⁴. Single crystal X-ray diffraction data on the set of as-grown and annealed crystals, with either $x=0.063$ or $x=0.146$, were collected on a Rigaku Pilatus 2000K diffractometer ($\text{Mo } K_{\alpha}$, $\lambda=0.71073 \text{ \AA}$). Crystals were mounted on MiTegen loops with a superglue for data collection at room temperature, with approximate sizes of $\sim 0.1 \times 0.1 \times 0.02 \text{ mm}^3$. Data processing and reduction were carried out using the CrystalClear⁶⁵ software package. Crystal structure of the parent compound BaFe_2As_2 with a fixed site occupancy ratio for Fe and Co atoms at the $4d$ site was used as the starting model in structural refinement. Crystal structures were refined to convergence using SHELX-2014⁶⁶.

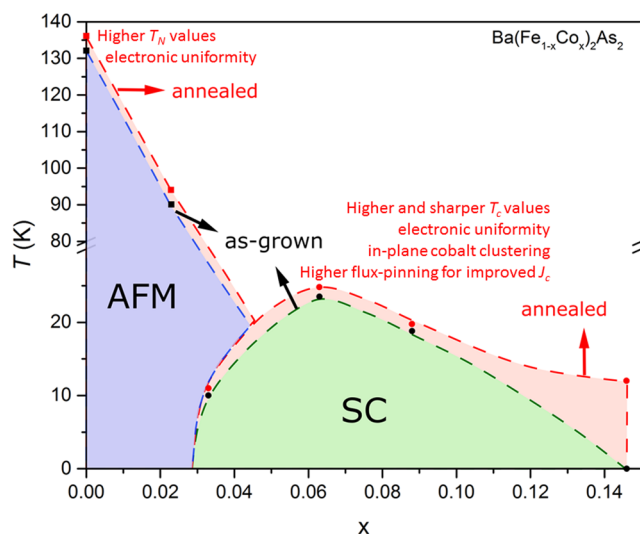


Figure 9. Annealing improves quantum transition temperatures in $\text{Ba}(\text{Fe}_{1-x}\text{Co}_x)_2\text{As}_2$ crystals. For all crystals, the overall lattice strain can be removed while the electronic structures become more uniform. While the in-plane cobalt chemical clustering can improve pinning, it seems to also raise the overall superconducting (SC) dome by giving paths for better percolation. Homogeneity improves antiferromagnetic transition temperatures (AFM).

Elemental analysis. The average chemical composition of each crystal was measured with a Hitachi S3400 scanning electron microscope operating at 20 kV, and use of energy-dispersive x-ray spectroscopy (EDS). For the line analysis on a crystal, the instrument used was the Hitachi S3400 Scanning electron Microscope operating at 20 kV. The beam current was set to provide approximately 1500 counts/second using a 10 mm² EDAX detector set for a processing time of 54 microsecond. Data were reduced using EDAX's Standardless Analysis program.

Neutron diffraction. For BaFe_2As_2 as-grown and annealed crystals, single-crystal neutron diffraction was performed on ~ 0.02 gram pieces, measured at the four-circle diffractometer HB-3A at the High Flux Isotope Reactor at ORNL. The neutron wavelength of 1.546 \AA was used from a Si-220 monochromator⁶⁷.

Physical property measurements. Temperature-dependent magnetic susceptibility (χ) data were collected on $\text{Ba}(\text{Fe}_{1-x}\text{Co}_x)_2\text{As}_2$ using a Quantum Design Magnetic Property Measurement System (MPMS), in zero-field-cooled or field-cooled modes, with field perpendicular to ab -plane at 10 Oe or 1 Tesla. Temperature-dependent electrical resistivity (ρ) or heat capacity (C) data were collected using a Physical Property Measurement System (PPMS). Hall coefficient (R_H) was calculated from the antisymmetric part of the transverse voltage perpendicular to the applied current under magnetic field ± 6 T reversal at fixed temperature. Critical current density (J_c) values were inductively (magnetically) determined by applying the modified critical state model^{68, 69} to the magnetic hysteresis via the relation $J_c = 20\Delta M/[a(1 - a/3b)]$. This relation applies to a rectangular solid with field perpendicular to a face with sides $b > a$. Sample dimensions were $1.52 \times 1.50 \times 0.162\text{ mm}^3$ for as-grown crystal, and $1.62 \times 1.69 \times 0.345\text{ mm}^3$ for annealed crystal. Here, $\Delta M = M^- - M^+$ is the magnetic hysteresis, where M^- (M^+) is the magnetization at temperatures T measured in decreasing (increasing) field H history. With these superconducting crystals in perpendicular field geometry, the flux density B can be replaced by $\mu_0 H$ to a close approximation. Fields in the range 0–6.5 T and in the c -direction were applied at different fixed temperatures (5 to 18.5 K) and the moment generated by the induced flowing current in the crystal was measured. Before beginning measurement, the magnet was reset to eliminate any trapped flux and assure zero H .

Transmission-electron-spectroscopy (TEM). Thin TEM specimens of $\text{Ba}(\text{Fe}_{1-x}\text{Co}_x)_2\text{As}_2$ parent and 0.063 were prepared by focused-ion-beam (FIB), and subsequently by ion milling with liquid nitrogen cooling at a weak beam of 1.5 kV and 3 mA. The conventional TEM and scanning STEM studies were carried out on an aberration-corrected FEI Titan S 80–300 equipped with a Gatan Image Filter (Quantum-865) at 300 kV. Z-contrast STEM-HAADF (high angle annular dark field) imaging was performed with a probe convergence angle of 30 mrad and an inner collection angle of 65 mrad. Electron-energy-loss-spectroscopy (EELS) data were collected in STEM mode using a dispersion of 0.25 eV per channel, a 5 mm aperture, and a collection angle of 40 mrad. Some EEL spectra and EELS mapping were acquired on a Nion UltraSTEM 100TM operating at 100 kV⁷⁰ equipped with a 5th order probe aberration corrector and a Gatan Enfina EEL spectrometer. STEM images of several micron areas on two pieces of each of as-grown versus annealed $x = 0.063$ were comparable.

Scanning-tunneling microscopy/spectroscopy (STM/S). Experiments are carried out with mechanically cut Pt-Ir tip in ultra-high vacuum variable temperature-STM chamber. The $x = 0$ crystals of as-grown and annealed were mounted on a moly plate side by side to do a direct comparison between the two by keeping all the experimental conditions same. The samples were cleaved *in situ* at ~ 120 K and immediately transferred to

STM head, which was precooled at 90 K. Topographic images are acquired in constant current mode with the bias voltage applied to the sample. Differential conductance (dI/dV) spectra were calculated numerically by taking derivative of current-voltage (I-V) measurements. For $x=0.063$ crystals, both as-grown and annealed pieces were cleaved *in situ* at ~ 100 K and then immediately transferred to STM head which was precooled at 4.2 K. Topographic images were acquired in constant current mode with the bias voltage applied to the sample. The dI/dV spectroscopies were obtained using the lock-in technique with bias modulation $V_{rms}=0.5$ mV at 973 Hz.

Theoretical calculations. We have performed calculations using the all-electron code WIEN2K⁷¹, within the local density approximation, and using the low-temperature orthorhombic structure.

References

1. Sefat, A. S. & Singh, D. J. Chemistry and electronic structure of iron-based superconductors. *MRS Bull.* **36**, 614–619 (2011).
2. Maple, M. B. Interplay between superconductivity and magnetism. *Phys. B Condens. Matter* **215**, 110–126 (1995).
3. Orenstein, J. & Millis, A. J. Advances in the Physics of High-Temperature Superconductivity. *Science* **288**, 468–474 (2000).
4. Ishida, K., Nakai, Y. & Hosono, H. To What Extent Iron-Pnictide New Superconductors Have Been Clarified: A Progress Report. *J. Phys. Soc. Jpn.* **78**, 62001-1-20 (2009).
5. Alloul, H., Bobroff, J., Gabay, M. & Hirschfeld, P. J. Defects in correlated metals and superconductors. *Rev. Mod. Phys.* **81**, 45–108 (2009).
6. Sefat, A. S. Pressure effects on two superconducting iron-based families. *Rep. Prog. Phys.* **74**, 124502-1-14 (2011).
7. Dai, P., Hu, J. & Dagotto, E. Magnetism and its microscopic origin in iron-based high-temperature superconductors. *Nat. Phys.* **8**, 709–718 (2012).
8. Konzen, L. M. N. & Sefat, A. S. Lattice parameters guide superconductivity in iron-arsenides. *J. Phys.: Condens. Matter* **29**, 083001-1-7 (2017).
9. Lumsden, M. D. & Christianson, A. D. Magnetism in Fe-based superconductors. *J. Phys.: Condens. Matter* **22**, 203203-1-26 (2011).
10. Sefat, A. S. *et al.* Superconductivity at 22 K in Co-Doped BaFe₂As₂ Crystals. *Phys. Rev. Lett.* **101**, 117004-1-4 (2008).
11. Sefat, A. S. *et al.* Structure and Anisotropic Properties of BaFe_{2-x}Ni_xAs₂ ($x=0, 1, 2$) Single Crystals. *Phys. Rev. B* **79**, 094508-1-8 (2009).
12. Rotundu, C. R. *et al.* Heat capacity study of BaFe₂As₂: Effects of annealing. *Phys. Rev. B* **82**, 144525-1-6 (2010).
13. Saparov, B. & Sefat, A. S. Annealing effects on the properties of BFe₂As₂ (B=Ca, Sr, Ba) superconducting parents. *Dalton Trans.* **43**, 14971–14975 (2014).
14. Rotter, M. *et al.* Spin-density-wave anomaly at 140 K in the ternary iron arsenide BaFe₂As₂. *Phys. Rev. B* **78**, 020503-1-4 (2008).
15. Gillett, J. *et al.* Dimensional Tuning of the Magnetic-Structural Transition in A(Fe_{1-x}Co_x)₂As₂ (A=Sr, Ba). arXiv:1005.1330, 1–5 (2010).
16. Gofryk, K. *et al.* Fermi-Surface Reconstruction and Complex Phase Equilibria in CaFe₂As₂. *Phys. Rev. Lett.* **112**, 186401-5 (2014).
17. Gofryk, K. *et al.* Effect of annealing on the specific heat of Ba(Fe_{1-x}Co_x)₂As₂. *Phys. Rev. B* **83**, 064513-1-8 (2011).
18. Gofryk, K. *et al.* Effect of annealing on the specific heat of optimally doped Ba(Fe_{0.92}Co_{0.08})₂As₂. *J. Phys.: Conf. Series* **273**, 012094-1-5 (2011).
19. Sun, D. L., Xiao, J. Z. & Lin, C. T. Growth and annealing effect of Co-doped BaFe₂As₂ single crystals. *J. Cryst. Growth* **321**, 55–59 (2011).
20. Mitchell, J. E. *et al.* Temperature-composition phase diagrams for Ba_{1-x}Sr_xFe₂As₂ ($0 \leq x \leq 1$) and superconducting Ba_{0.5}Sr_{0.5}(Fe_{1-y}Co_y)₂As₂ ($0 \leq y \leq 0.141$). *Phys. Rev. B* **86**, 174511-1-9 (2012).
21. Berlijn, T., Lin, C. H., Garber, W. & Ku, W. Do Transition-Metal Substitutions Dope Carriers in Iron-Based Superconductors. *Phys. Rev. Lett.* **108**, 207003-1-5 (2012).
22. Gofryk, K. *et al.* Local Inhomogeneity and Filamentary Superconductivity in Pr-Doped CaFe₂As₂. *Phys. Rev. Lett.* **112**, 047005-1-5 (2014).
23. Sefat, A. S. Pressure effects on two superconducting iron-based families. *Rep. Prog. Phys.* **74**, 124502-1-14 (2011).
24. Dhital, C. *et al.* Effect of Uniaxial Strain on the Structural and Magnetic Phase Transitions in BaFe₂As₂. *Phys. Rev. Lett.* **108**, 087001-1-4 (2012).
25. Bianconi, A. and Saini, N. L. In Superconductivity in Complex Systems, eds Müller, K. A. and Bussmann-Holder, A. (Springer: Berlin, Heidelberg, New York), 114, 287–330 (2005).
26. Wise, W. D. *et al.* Imaging nanoscale Fermi-surface variations in an inhomogeneous superconductor. *Nat. Phys.* **5**, 213–216 (2009).
27. Allan, M. P. *et al.* Anisotropic impurity states, quasiparticle scattering and nematic transport in underdoped Ca(Fe_{1-x}Co_x)₂As₂. *Nat. Phys.* **9**, 220–224 (2013).
28. Campi, G. *et al.* Inhomogeneity of charge-density-wave order and quenched disorder in a high- T_c superconductor. *Nature* **525**, 359–362 (2015).
29. Chen, F. *et al.* Electronic Identification of the Parental Phases and Mesoscopic Phase Separation of K_xFe_{2-y}Se₂ Superconductors. *Phys. Rev. X* **1**, 021020-1-8 (2011).
30. Li, W. *et al.* Phase separation and magnetic order in K-doped iron selenide superconductor. *Nature Phys.* **8**, 126–130 (2012).
31. Ricci, A. *et al.* Intrinsic phase separation in superconducting K_{0.8}Fe_{1.6}Se₂ ($T_c=31.8$ K) single crystals. *Supercond. Sci. Technol.* **24**, 082002-1-7 (2011).
32. Yuan, R. H. *et al.* Nanoscale phase separation of antiferromagnetic order and superconductivity in K_{0.75}Fe_{1.75}Se₂. *Sci. Rep.* **2**, 221-1-5 (2012).
33. Ricci, A. *et al.* Nanoscale phase separation in the iron chalcogenide superconductor K_{0.8}Fe_{1.6}Se₂ as seen via scanning nanofocused x-ray diffraction. *Phys. Rev. B* **84**, 060511-1-4 (2011).
34. Ni, N. *et al.* Effects of Co substitution on thermodynamic and transport properties and anisotropic H_{c2} in Ba(Fe_{1-x}Co_x)₂As₂ single crystals. *Phys. Rev. B* **78**, 214515-1-9 (2008).
35. Mun, E. D., Bud'ko, S. L., Ni, N., Thaler, A. N. & Canfield, P. C. Thermoelectric power and Hall coefficient measurements on Ba(Fe_{1-x}T_x)₂As₂ (T=Co and Cu). *Phys. Rev. B* **80**, 054517-1-6 (2009).
36. Rullier-Albenque, F., Colson, D., Forget, A. & Alloul, H. Hall Effect and Resistivity Study of the Magnetic Transition, Carrier Content, and Fermi-Liquid Behavior in Ba(Fe_{1-x}Co_x)₂As₂. *Phys. Rev. Lett.* **103**, 057001-1-4 (2009).
37. Marty, K. *et al.* Competing magnetic ground states in nonsuperconducting Ba(Fe_{1-x}Cr_x)₂As₂ as seen via neutron diffraction. *Phys. Rev. B* **83**, 060509-1-4 (2011).
38. Li, L. *et al.* Role of magnetism in superconductivity of BaFe₂As₂: Study of 5d Au-doped crystals. *Phys. Rev. B* **92**, 094504-1-7 (2015).
39. Forrest, T. R., Valdivia, P. N., Rotundu, C. R., Bourret-Courchesne, E. & Birgeneau, R. J. The effects of post-growth annealing on the structural and magnetic properties of BaFe₂As₂. *J. Phys.: Condens. Matter* **28**, 115702-1-8 (2016).
40. Jin, R. *et al.* Electronic, magnetic and optical properties of two Fe-based superconductors and related parent compounds. *Supercond. Sci. Technol.* **23**, 054005-1-6 (2010).

41. Massee, F. *et al.* Nanoscale superconducting gap variations and lack of phase separation in optimally doped BaFe_{1.86}Co_{0.14}As₂. *Phys. Rev. B* **79**, 220517-1-4 (2009).
42. Ziatdinov, M. *et al.* Deep data mining in a real space: separation of intertwined electronic responses in a lightly doped BaFe₂As₂. *Nanotechnology* **27**, 475706-1-9 (2016).
43. Cantoni, C. *et al.* Orbital Occupancy and Charge Doping in Iron-Based Superconductors. *Adv. Mater.* **26**, 6193–6198 (2014).
44. Saparov, B. *et al.* Complex structures of different CaFe₂As₂ samples. *Sci. Rep.* **4**, 4120-1-7 (2014).
45. Sefat, A. S. *et al.* Anomalous magneto-elastic and charge doping effects in thallium-doped BaFe₂As₂. *Sci. Rep.* **6**, 21660-1-9 (2016).
46. Yamamoto, A. *et al.* Small anisotropy, weak thermal fluctuations, and high field superconductivity in Co-doped iron pnictide Ba(Fe_{1-x}Co_x)₂As₂Ba(Fe_{1-x}Co_x)₂As₂. *Appl. Phys. Lett.* **94**, 62511-1-3 (2009).
47. Yang, H., Luo, H., Wang, Z. & Wen, H.-H. Fishtail effect and the vortex phase diagram of single crystal Ba_{0.6}K_{0.4}Fe₂As₂. *Appl. Phys. Lett.* **93**, 142506-1-3 (2008).
48. Prozorov, R. *et al.* Vortex phase diagram of Ba(Fe_{0.93}Co_{0.07})₂As₂ single crystals. *Phys. Rev. B* **78**, 224506-1-11 (2008).
49. Sun, D. L., Liu, Y. & Lin, C. T. Comparative study of upper critical field H_{c2} and second magnetization peak H_{sp} in hole- and electron-doped BaFe₂As₂ superconductor. *Phys. Rev. B* **80**, 144515-1-6 (2009).
50. Putti, M. *et al.* New Fe-based superconductors: properties relevant for applications. *Supercond. Sci. Technol.* **23**, 34003-1-10 (2010).
51. Katase, T., Hiramatsu, H., Kamiya, T. & Hosono, H. High Critical Current Density 4MA/cm² in Co-Doped BaFe₂As₂ Epitaxial Films Grown on (La, Sr)(Al, Ta)O_x Substrates without Buffer Layers. *Appl. Phys. Express* **3**, 63101-1-3 (2010).
52. Blatter, G., Feigel'man, M. V., Geshkenbein, V. B., Larkin, A. I. & Vinokur, V. M. Vortices in high-temperature superconductors. *Rev. Mod. Phys.* **66**, 1125–1388 (1994).
53. Hoffman, J. E. Spectroscopic scanning tunneling microscopy insights into Fe-based superconductors. *Rep. Prog. Phys.* **74**, 124513-1-34 (2011).
54. Massee, F. *et al.* Pseudogap-less high-T_c superconductivity in BaCo_xFe_{2-x}As₂. *Europhys. Lett.* **92**, 57012-1-5 (2010).
55. Yin, Y. *et al.* Scanning Tunneling Spectroscopy and Vortex Imaging in the Iron Pnictide Superconductor BaFe_{1.8}Co_{0.2}As₂. *Phys. Rev. Lett.* **102**, 097002-1-4 (2009).
56. Dynes, R. C., Narayananur, V. & Gurno, J. P. Direct Measurement of Quasiparticle-Lifetime Broadening in a Strong-Coupled Superconductor. *Phys. Rev. Lett.* **41**, 1509–1512 (1978).
57. Pakokthom, C., Krunkavakarn, B., Udomsuthirun, P. & Yoksan, S. Reduced Gap Ratio of High-T_c Cuprates Within the d-Wave Two-Dimensional Van Hove Scenario. *J. Supercond.* **11**, 429–432 (1998).
58. Shan, L. *et al.* Evidence of multiple nodeless energy gaps in superconducting Ba_{0.6}K_{0.4}Fe₂As₂ single crystals from scanning tunneling spectroscopy. *Phys. Rev. B* **83**, 60510-1-4 (2011).
59. Teague, M. L. *et al.* Measurement of a Sign-Changing Two-Gap Superconducting Phase in Electron-Doped Ba(Fe_{1-x}Co_x)₂As₂ Single Crystals Using Scanning Tunneling Spectroscopy. *Phys. Rev. Lett.* **106**, 87004-1-4 (2011).
60. Yin, Y. *et al.* Scanning Tunneling Spectroscopy and Vortex Imaging in the Iron Pnictide Superconductor BaFe_{1.8}Co_{0.2}As₂. *Phys. Rev. Lett.* **102**, 97002-1-4 (2009).
61. Zhang, H. *et al.* $\sqrt{2} \times \sqrt{2}$ structure and charge inhomogeneity at the surface of superconducting BaFe_{2-x}Co_xAs₂ (x=0–0.32). *Phys. Rev. B* **81**, 104520-1-5 (2010).
62. Gozar, A. *et al.* High-temperature interface superconductivity between metallic and insulating copper oxides. *Nature* **455**, 782–85 (2008).
63. Sefat, A. S. Bulk synthesis of iron-based superconductors. *Curr. Opin. Solid State Mater. Sci.* **17**, 59–64 (2013).
64. Akselrud, L. & Grin, Y. WinCSD: software package for crystallographic calculations (Version 4). *J. Appl. Crystallogr.* **47**, 803–805 (2014).
65. Rigaku/MSC, *CrystalClear 2.0*. Rigaku/MSC Inc., The Woodlands, Texas, USA (2014).
66. Sheldrick, G. M. Crystal structure refinement with SHELXL. *Acta Crystallogr. Sect. C Struct. Chem.* **71**, 3–8 (2015).
67. Chakoumakos, B. C. *et al.* Four-circle single-crystal neutron diffractometer at the High Flux Isotope Reactor. *J. Appl. Crystallogr.* **44**, 655–658 (2011).
68. Bean, C. P. Magnetization of High-Field Superconductors. *Rev. Mod. Phys.* **36**, 31–39 (1964).
69. Bean, C. P. Magnetization of Hard Superconductors. *Phys. Rev. Lett.* **8**, 250–253 (1962).
70. Krivanek, O. L. *et al.* An electron microscope for the aberration-corrected era. *Ultramicroscopy* **108**, 179–195 (2008).
71. Blaha, P., Schwarz, K., Madsen, G., Kvasnicka, D. and Luitz, J. WIEN2k, An augmented plane wave + local orbitals program for calculating crystal properties (Karlheinz Schwarz, Techn. Universität Wien, Austria 2001).

Acknowledgements

The research is primarily supported by the U.S. Department of Energy (DOE), Office of Science, Basic Energy Sciences (BES), Materials Science and Engineering Division. The spectroscopy and microscopy work was performed through user projects supported by the ORNL's Center for Nanophase Materials Sciences (CNMS), which is sponsored by an Office of Science User Facility, DOE. A.O.I. work was supported by the U.S. Department of Energy, Office of Science, Office of Workforce Development for Teachers and Scientists (WDTS) under the VFP. The single-crystal neutron and X-ray diffraction work at ORNL were sponsored by the Scientific User Facilities Division, Office of BES, DOE. Z.W. work was supported by the National Natural Science Foundations of China (no. 61227009). The authors acknowledge assistance by J. Mitchell, Z. Sims, and M. Susner for some of the sample preparations, and also L. Walker for composition line analysis on a crystal. We also thank C. Hoffman and S. Kalinin for discussions.

Author Contributions

L.L. prepared the samples and carried out most of the bulk property measurements. Q. Zheng and M.C. performed TEM and EELS experiments. Q. Zou, S.R., Z.W., and Z.G. made STM/S measurements. S.S. and S.J. did quantitative spatial analyses of electronic structure. A.O.I. performed magnetization measurements for J_c analyses. X.P.W. and H.B.C. did single-crystal X-ray, and neutron diffractions, respectively. D.P. did theoretical calculations. A.S. supervised the experiments and discussions, assisted in analyses of results, and wrote the paper. All authors reviewed the manuscript, and contributed to the analyses, and writing of the manuscript.

Additional Information

Competing Interests: The authors declare that they have no competing interests.

Publisher's note: Springer Nature remains neutral with regard to jurisdictional claims in published maps and institutional affiliations.



Open Access This article is licensed under a Creative Commons Attribution 4.0 International License, which permits use, sharing, adaptation, distribution and reproduction in any medium or format, as long as you give appropriate credit to the original author(s) and the source, provide a link to the Creative Commons license, and indicate if changes were made. The images or other third party material in this article are included in the article's Creative Commons license, unless indicated otherwise in a credit line to the material. If material is not included in the article's Creative Commons license and your intended use is not permitted by statutory regulation or exceeds the permitted use, you will need to obtain permission directly from the copyright holder. To view a copy of this license, visit <http://creativecommons.org/licenses/by/4.0/>.

© The Author(s) 2017